nature communications

Article

https://doi.org/10.1038/s41467-025-61232-z

Modulating Ru-Co bond lengths in Ru_1Co single-atom alloys through crystal phase engineering for electrocatalytic nitrate-to-ammonia conversion

Received: 30 October 2024

Accepted: 13 June 2025

Published online: 01 July 2025

Check for updates

Xiaojuan Zhu[1,5], Yi-Chi Wang[2,5], Kaiyu Qu[1], Leyang Song[1], Jing Wang[1], Yushuang Gong[1], Xiang Liu[1], Cheng-Fei Li[3], Shiling Yuan[1], Qipeng Lu[4] ✉ & An-Liang Wang[1] ✉

Single atom alloys (SAAs) with maximum atomic efficiency and uniform active sites show great promise for heterogeneous catalytic applications. Meanwhile, crystal phase engineering has granered significant interest due to tailored atomic arrangements and coordination environments. However, the crystal phase engineering of SAAs remains challenging owing to high surface energy and complex phase transition dynamics. Herein, Ru_1Co SAAs with tunable crystal phases (hexagonal-close-packed (hcp), face-centered-cubic (fcc), and hcp/fcc structure) are successfully synthesized via controlled phase transitions. These SAAs exhibit distinct crystal phase-dependent performance towards nitrate reduction reaction (NO_3RR), where hcp-Ru_1Co outperforms its counterparts with a NH_3 Faradaic efficiency of 96.78% at 0 V vs. reversible hydrogen electrode and long-term stability exceeding 1200 h. Mechanistic investigations reveal that the hcp configurations enables shorter Ru-Co distances, stronger interatomic interactions, and more positive surface potential compared to hcp/fcc-Ru_1Co and fcc-Ru_1Co, which enhances the NO_3^- adsorption, reduces the free energy barrier, and suppresses competitive hydrogen evolution.

Noble metal-based nanomaterials have attracted considerable attention in electrocatalysis due to their unique catalytic properties[1,2]. Theoretically, modulating the crystal structure can tailor the coordination geometry and electronic configuration of active sites, thereby affecting the adsorption/desorption behavior of reactants and intermediates, which ultimately regulates catalytic performance[3,4]. However, the inherent characteristics of metallic bonds (their unsaturated and non-directional nature) tend to drive metal catalysts toward conventional crystal structures[5,6]. For instance, Ru typically forms a hexagonal-close-packed (hcp) structure while Pt adopts a face-centered-cubic (fcc) arrangement. This structural persistence presents significant challenges in both controlling crystal phase modifications and establishing clear structure–property relationships in metallic catalytic systems.

To minimize noble metal usage while enhancing catalytic performance, the atomic dispersion of noble metal atoms within a host

[1]Key Laboratory for Colloid and Interface Chemistry, Ministry of Education, School of Chemistry and Chemical Engineering, Shandong University, Jinan, China. [2]Beijing National Center for Electron Microscopy and Laboratory of Advanced Materials, School of Materials Science and Engineering, Tsinghua University, Beijing, China. [3]National Energy Key Laboratory for New Hydrogen-Ammonia Energy Technologies, Foshan Xianhu Laboratory, Foshan, China. [4]School of Materials Science and Engineering, University of Science and Technology Beijing, Beijing, China. [5]These authors contributed equally: Xiaojuan Zhu, Yi-Chi Wang. ✉e-mail: qipeng@ustb.edu.cn; alwang@sdu.edu.cn

metal matrix to form single-atom-alloys (SAAs) has emerged as an effective strategy[7–9]. SAAs can realize the maximum utilization of metal atoms, uniform active sites, peculiar geometric and electronic structures, which collectively contribute to superior catalytic properties[10–13]. The well-defined active centers in SAAs further facilitate fundamental investigations of structure–activity relationships and catalytic mechanisms. Nevertheless, constructing SAAs with tailored crystal structures remains challenging due to the high surface energy of isolated metal atoms and the lack of effective synthetic methods for precise crystal phase control at the nanoscale. Notably, successful demonstrations of crystal phase engineering in SAAs have not yet been reported.

Herein, we successfully synthesize Ru_1Co SAAs with distinct crystal phases (i.e., hcp-Ru_1Co, hcp/fcc-Ru_1Co, and fcc-Ru_1Co) through a solvothermal method followed by thermal annealing. These obtained Ru_1Co SAAs are employed as electrocatalysts for nitrate reduction reaction (NO_3RR) to ammonia (NH_3). Remarkably, hcp-Ru_1Co demonstrates competitive performance with a NH_3 Faradaic efficiency (FE_{NH_3}) of 96.78% at 0 V vs. reversible hydrogen electrode (RHE). The energy consumption (EC) and NH_3 production cost for hcp-Ru_1Co are calculated as 19.04 kWh kg^{-1} and 0.57 $\$_{USD}$ kg^{-1}, respectively. Additionally, hcp-Ru_1Co maintains operational stability for over 1200 h. Combined experimental and theoretical analyses reveal that hcp-Ru_1Co possesses reduced Ru–Co distances, enhanced Ru–Co interatomic interactions, and more positive surface potential compared to hcp/fcc-Ru_1Co and fcc-Ru_1Co, collectively promoting NO_3^- adsorption, lowering the free energy barrier, and suppressing hydrogen evolution reaction (HER). A prototype Zn-NO_3^- battery employing hcp-Ru_1Co as the cathode catalyst demonstrates high electrochemical performance.

Results

Synthesis and structural characterizations

The Ru_1Co SAAs with different crystal phases are successfully synthesized via a solvothermal method followed by thermal annealing (see the "Methods" section for experimental details and Fig. 1a for schematic illustration). Specifically, $CoCl_2{\cdot}6H_2O$ and $RuCl_3{\cdot}xH_2O$ precursors are dissolved in 1,4-butanediol and heated at 230 °C for 20 min. Subsequent annealing at 300, 500, and 700 °C for 30 min yields hcp-Ru_1Co, hcp/fcc-Ru_1Co, and fcc-Ru_1Co, respectively.

The crystal phases of synthesized samples are characterized by X-ray diffraction (XRD). As shown in Fig. 1b, d, the diffraction peaks of hcp-Ru_1Co match well with those of hcp-Co (JCPDS No. 05-0727), while fcc-Ru_1Co exhibits the diffraction peaks well indexed to fcc-Co (JCPDS No. 15-0806). Notably, the diffraction peaks of both hcp-Ru_1Co and fcc-Ru_1Co exhibit slightly negative shifts compared to those of hcp-Co and fcc-Co, indicating the successful incorporation of Ru with a large atomic radius into the Co matrix. The XRD pattern of hcp/fcc-Ru_1Co shows the coexistence of diffraction peaks from both phases (Fig. 1c), verifying the successful synthesis of hcp/fcc-Ru_1Co. Rietveld refinement profiles demonstrate high phase purity in all Ru_1Co SAAs. Inductively coupled plasma-optical emission spectroscopy (ICP-OES) analysis confirms consistent Co/Ru atomic ratios of 99.25/0.75 in all Ru_1Co SAAs (Supplementary Table 1).

The morphology of hcp-Ru_1Co is investigated through transmission electron microscopy (TEM) and high-angle annular dark-field scanning TEM (HAADF-STEM), which reveals a homogeneous nano-urchin structure (Fig. 2a, Supplementary Figs. 1 and 2). Atomic-scale characterization via aberration-corrected HAADF-STEM (AC-HAADF-STEM) utilizes Z-contrast imaging, where Ru atoms ($Z = 44$) exhibit brighter atomic-scale contrast compared to Co ($Z = 27$). As shown in Fig. 2b, isolated Ru atoms are observed without detectable clusters or nanoparticles, confirming the atomic dispersion of Ru in the Co matrix. Three-dimensional (3D) surface plots converted from the cyan square in Fig. 2b are analyzed. High-intensity spots represent Ru atoms, while low-intensity spots correspond to Co atoms. The isolated Ru spots in Fig. 2c provide additional evidence of Ru atomic dispersion. The atomic arrangement of hcp-Ru_1Co is further revealed by high-resolution AC-HAADF-STEM (Fig. 2d). An enlarged view from the cyan square in Fig. 2d shows the atomic columns along the [110] zone axis (Fig. 2e), closely matching the simulated atomic model of hcp-Co (Fig. 2g). The corresponding fast Fourier transform (FFT) pattern (Fig. 2f) aligns with the simulated electron diffraction pattern of hcp-Co (Fig. 2h). Interplanar spacings measured from the intensity profiles (converted from orange rectangles in Fig. 2d) are 0.21 and 0.19 nm, corresponding to the (110) and (111) planes of hcp-Ru_1Co, respectively (Fig. 2i, j). Notably, the presence of isolated peaks with relatively high intensity further confirms the atomic dispersion of Ru. HAADF-STEM image and corresponding elemental mappings demonstrate the uniform distribution of Ru and Co in the nano-urchin structure (Fig. 2k–n). Energy-dispersive X-ray spectroscopy (EDS) reveals the Ru/Co atomic ratio of 99.24/0.76 (Supplementary Fig. 3), consistent with ICP-OES results.

The structural characteristics of fcc-Ru_1Co are systematically investigated. TEM image confirms the preserved nano-urchin morphology (Fig. 3a and Supplementary Fig. 4). Atomic dispersion of Ru in the Co matrix is verified by HAADF-STEM (Fig. 3b) and 3D surface plot analysis (Fig. 3c). An enlarged AC-HAADF-STEM image (Fig. 3e) from the purple square in Fig. 3d shows the atomic columns along the [110] zone axis, matching the simulated atomic model of fcc-Co (Fig. 3g). The corresponding FFT pattern (Fig. 3f) aligns with the simulated diffraction pattern of fcc-Co (Fig. 3h). Interplanar spacing measurements yield 0.21 nm, corresponding to the (111) plane of fcc-Ru_1Co, with isolated Ru peaks confirming atomic dispersion (Fig. 3i, j). For hcp/fcc-Ru_1Co, TEM image reveals the conserved nano-urchin structure (Fig. 3k and Supplementary Fig. 5). HAADF-STEM image (Fig. 3l) and 3D surface plots (Fig. 3m) confirm the atomic dispersion of Ru. High-resolution AC-HAADF-STEM image reveals two types of atomic arrangements with distinct heterophase boundary (Fig. 3n). FFT patterns (Fig. 3o and p) from the selected purple and cyan squares in Fig. 3n, align with the simulated diffraction patterns of fcc-Co along the [110] zone axis (Fig. 3q) and hcp-Co along the [111] zone axis (Fig. 3r), respectively. FFT pattern (Supplementary Fig. 6b) from the boundary region (orange square) in Supplementary Fig. 6a, reveals the overlapped electron diffraction dots along the [110] zone axis of fcc-Co ($[110]_{fcc}$) and the [111] zone axis of hcp-Co ($[111]_{hcp}$) (Supplementary Fig. 6c). The intensity profiles from the orange rectangles in Fig. 3n reveal the interplanar spacings of 0.21 and 0.20 nm, assigned to the (111) plane of fcc-Ru_1Co and (011) plane of hcp-Ru_1Co, respectively (Fig. 3s, t). The existence of the isolated maximum peaks further confirms Ru atomic dispersion.

The electronic structure and coordination environment of Ru_1Co SAAs with different crystal phases are investigated by X-ray photoelectron spectroscopy (XPS) and X-ray absorption spectroscopy (XAS). XPS analysis confirms that metallic Co and Ru are dominant in all Ru_1Co SAAs (Supplementary Fig. 7). The Ru 3p XPS spectrum of hcp-Ru_1Co exhibits peaks at 461.38 and 483.56 eV, assigned to $3p_{3/2}$ and $3p_{1/2}$ of Ru^0, respectively[14]. A positive shift in the binding energy of Ru^0 $3p_{3/2}$ peak is observed for hcp/fcc-Ru_1Co (461.79 eV) and fcc-Ru_1Co (462.01 eV) compared to hcp-Ru_1Co (461.38 eV), suggesting reduced electron density on Ru in hcp-Ru_1Co. The observed oxides are attributed to the easy oxidation characters of Co and Ru in air, in accordance with previous reports[15,16]. Figure 4a displays the normalized Co K-edge X-ray absorption near edge structure (XANES) spectra of Ru_1Co SAAs and references (i.e., Co foil and Co_3O_4). The absorption edges of all Ru_1Co SAAs are close to Co foil but with slight shifts towards higher energy, indicating the metallic characteristics of Co with reduced electron density. This is attributed to the lower electronegativity of Co (1.9) compared to Ru (2.2), resulting in electron transfer from Co to Ru[17]. This directional electron transfer is further corroborated by the decreased valence state of Ru in hcp-Ru_1Co, hcp/fcc-Ru_1Co, and

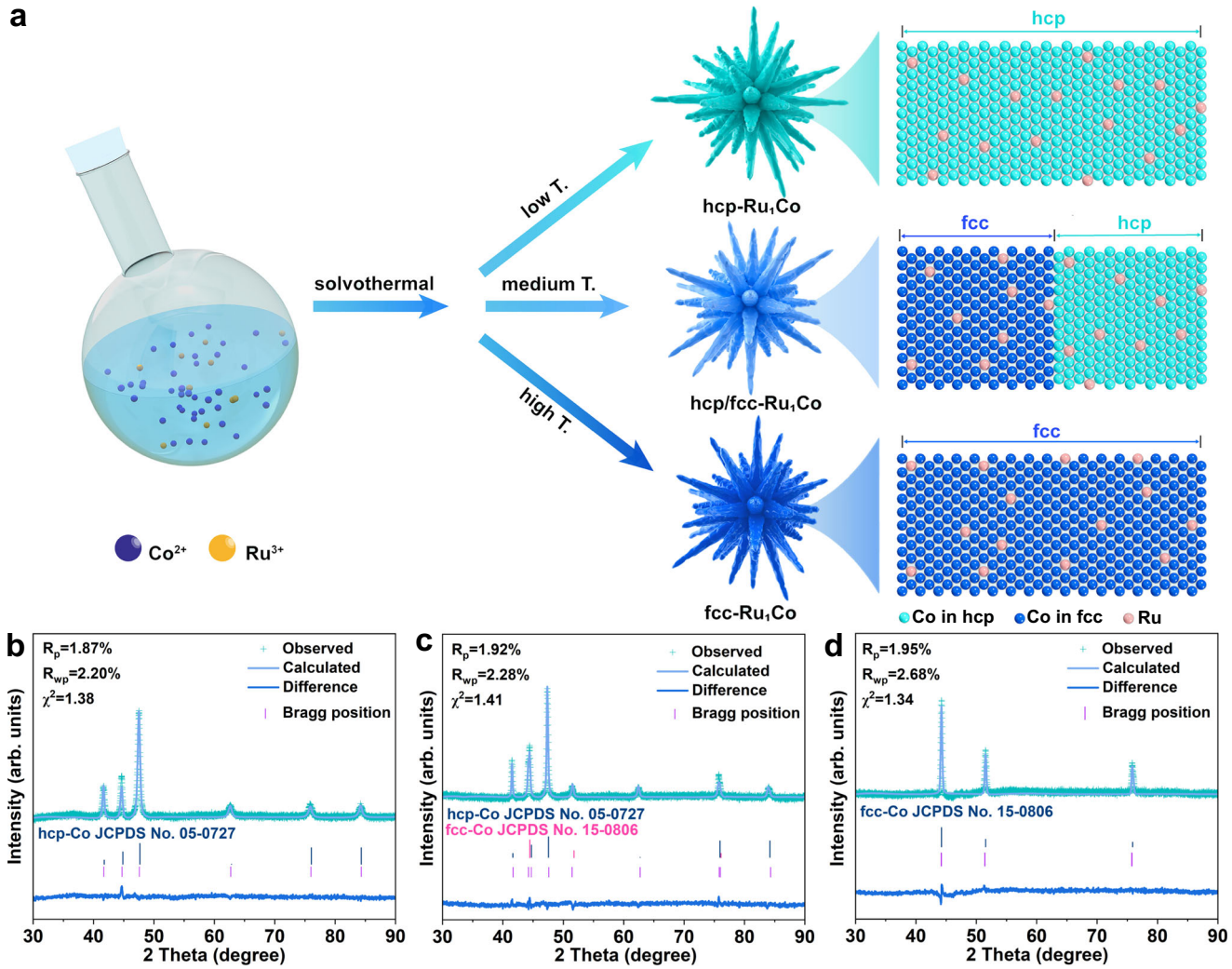

Fig. 1 | Scheme and XRD characterization. a Scheme for the formation of Ru_1Co SAAs with different crystal phases. **b**–**d** The Rietveld refinement of XRD patterns of hcp-Ru_1Co (**b**), hcp/fcc-Ru_1Co (**c**), and fcc-Ru_1Co (**d**). Source data for this figure are provided as a Source Data file.

fcc-Ru_1Co relative to Ru foil, as revealed in the normalized Ru K-edge XANES spectra (Fig. 4c). Notably, the Co K-edge adsorption of hcp-Ru_1Co positively shifts compared to fcc-Ru_1Co and hcp/fcc-Ru_1Co (inset of Fig. 4a), with the opposite trend observed for the Ru K-edge adsorption (inset of Fig. 4c), suggesting a stronger electronic interaction between Co and Ru in hcp-Ru_1Co.

Extended X-ray absorption fine structure (EXAFS) spectroscopy is performed to probe the local atomic configurations. The Co K-edge Fourier transformed EXAFS (FT-EXAFS) spectra of Ru_1Co SAAs display a prominent peak at 2.17 Å, matching the characteristic Co–Co bond observed in Co foil (Fig. 4b). This consistent peak position results from the low Ru concent and the predominant Co–Co bond in Ru_1Co SAAs. The Ru K-edge FT-EXAFS spectrum of Ru foil shows a peak at 2.35 Å, corresponding to the Ru–Ru metallic bond (Fig. 4d). In contrast, hcp-Ru_1Co, hcp/fcc-Ru_1Co, and fcc-Ru_1Co exhibit the prominent peaks at 2.10, 2.13, and 2.17 Å, respectively. The significant differences in peak positions between Ru foil and Ru_1Co SAAs suggest that the prominent peak of Ru_1Co SAAs is not contributed by Ru–Ru metallic bond, but Ru–Co metallic bond. The absence of Ru–Ru bond further confirms the atomic dispersion of Ru in Ru_1Co SAAs. Notably, the Ru–Co bond length in hcp-Ru_1Co is shorter than that in fcc-Ru_1Co and hcp/fcc-Ru_1Co, suggesting enhanced interatomic interactions between Ru and Co in hcp-Ru_1Co, consistent with the XANES results.

The least-squares EXAFS fitting curves and fitting parameters are provided in Supplementary Figs. 8–17 and Tables 2 and 3. The Co K-edge EXAFS oscillation functions reveal minor variations in both oscillation frequencies and amplitudes for hcp-Ru_1Co, hcp/fcc-Ru_1Co, and fcc-Ru_1Co, indicating similar coordination environment for Co species (Supplementary Fig. 18). In contrast, the Ru K-edge EXAFS oscillation functions of Ru_1Co SAAs exhibit significant differences, reflecting substantial variations induced by crystal phase differences (Fig. 4e). The Co K-edge wavelet-transformed EXAFS (WT-EXAFS) contour plot of Co foil shows a local maximum at $k = 7.21$ Å^{-1} and $R = 2.17$ Å, similar to that of hcp-Ru_1Co ($k = 7.25$ Å^{-1}, $R = 2.17$ Å), hcp/fcc-Ru_1Co ($k = 7.42$ Å^{-1}, $R = 2.17$ Å), and fcc-Ru_1Co ($k = 7.59$ Å^{-1}, $R = 2.17$ Å) (Supplementary Fig. 19). However, the Ru K-edge WT-EXAFS contour plot reveals that hcp-Ru_1Co exhibits a local maximum at $k = 7.69$ Å^{-1} and $R = 2.10$ Å, which is significantly different from Ru foil ($k = 9.52$ Å^{-1}, $R = 2.35$ Å) and assigned to Ru–Co bond (Fig. 4f, i). Additionally, the lower R value in hcp-Ru_1Co (2.10 Å) in comparison with hcp/fcc-Ru_1Co (2.13 Å) and fcc-Ru_1Co (2.17 Å) further confirms the shorter Ru–Co bond in hcp-Ru_1Co (Fig. 4g, h). These results collectively confirm that hcp-Ru_1Co possesses a shorter Ru–Co bond and thus stronger interatomic interaction compared to hcp/fcc-Ru_1Co and fcc-Ru_1Co.

To further confirm the atomic dispersion of Ru in Ru_1Co SAAs with different crystal phases, in situ CO diffuse reflectance infrared Fourier transform spectroscopy (CO-DRIFTS) is performed (Fig. 4j and

https://doi.org/10.1038/s41467-025-61232-z

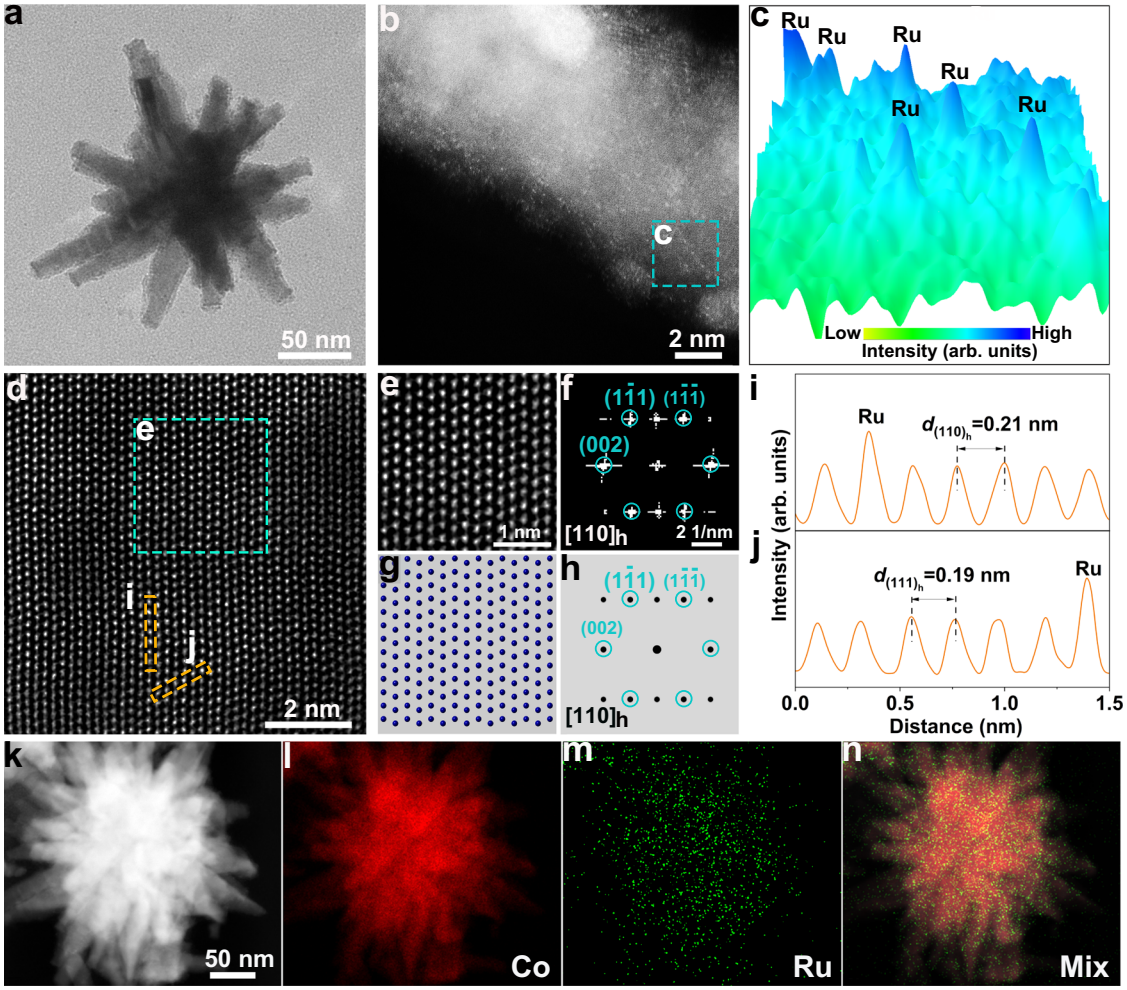

Fig. 2 | Characterization of hcp-Ru$_1$Co. a TEM image of hcp-Ru$_1$Co. **b** HAADF-STEM image of hcp-Ru$_1$Co. **c** 3D surface plots converted from the cyan square in (**b**). **d** High-resolution AC-HAADF-STEM image of hcp-Ru$_1$Co. **e** Enlarged AC-HAADF-STEM image taken from the cyan square in (**d**). **f** The corresponding FFT pattern. **g** and **h** The simulated atomic model (**g**) and the electron diffraction pattern (**h**) of hcp-Co viewed along the [110] zone axis. **i** and **j** Intensity profiles from the orange rectangles in (**d**). **k**–**n** HAADF-STEM image (**k**) and corresponding elemental mappings (**l**–**n**) of hcp-Ru$_1$Co. Source data for this figure are provided as a Source Data file.

Supplementary Fig. 20). Following CO adsorption at room temperature, two broad peaks at 2170 and 2121 cm^{-1} are observed, corresponding to the mononuclear (Ru$^{\delta+}$(CO)) and tricarbonyl species adsorbed on single Ru atom (Ru$^{\delta+}$(CO)$_3$), respectively[18–20]. The absence of peaks below 2000 cm^{-1}, which is the fingerprint of bridge-bonded CO, confirms the absence of Ru clusters or nanoparticles[21,22].

Electrocatalytic NO_3RR performance

The electrocatalytic NO_3RR performance is evaluated using an H-type cell. Ru$_1$Co SAAs supported on Ni foam (NF) serve as the working electrode, with Ag/AgCl (saturated KCl) and Pt wire as the reference and counter electrodes, respectively. The electrolyte contains 0.5 M Na_2SO_4 and 0.1 M NaOH with 200 ppm NO_3^--N. All potentials are referenced to the RHE scale. Figure 5a displays the linear sweep voltammetry (LSV) curves of Ru$_1$Co SAAs in electrolyte with/without 200 ppm NO_3^--N. Apparently, upon the addition of NO_3^-, significant enhancement in current density is observed, indicating the occurrence of NO_3RR. Notably, hcp-Ru$_1$Co demonstrates the highest current density in the presence of NO_3^- and the lowest current density in the absence of NO_3^-, indicating superior NO_3RR activity and suppressed hydrogen evolution reaction (HER) (Supplementary Fig. 21).

The NO_3RR performance of Ru$_1$Co SAAs is systematically investigated through chronoamperometric tests at different potentials. The concentrations of NO_3^--N and NH_4^+-N are quantified by colorimetric methods via UV–Vis spectrophotometer (Supplementary Figs. 22 and 23). As shown in Fig. 5b and Supplementary Fig. 24, hcp-Ru$_1$Co exhibits superior performance with maximum NH_3 yield rate (Y_{NH_3}) of 1.33 ± 0.06 mg h^{-1} cm^{-2} at −0.1 V and NH_3 Faradaic efficiency (FE_{NH_3}) of 96.78 ± 1.97% at 0 V, significantly outperforming hcp/fcc-Ru$_1$Co (0.90 ± 0.06 mg h^{-1} cm^{-2}, 84.41 ± 3.70%) and fcc-Ru$_1$Co (0.39 ± 0.05 mg h^{-1} cm^{-2}, 56.94 ± 2.60%). The minimal concentrations of by-products (i.e., NO_2^-, N_2H_4, N_2, and H_2) confirm the high NH_3 selectivity of hcp-Ru$_1$Co (Supplementary Figs. 25–31). At 0 V, hcp-Ru$_1$Co demonstrates higher values of Y_{NH_3}, FE_{NH_3}, NO_3^- conversion ($C_{NO_3^-}$), NH_3 selectivity (S_{NH_3}), half-cell energy efficiencies of NH_3 (EE_{NH_3}) and NH_3 partial current density (j_{NH_3}) compared to hcp/fcc-Ru$_1$Co and fcc-Ru$_1$Co (Fig. 5c and Supplementary Figs. 32 and 33). Notably, under high-concentration conditions (1400 ppm NO_3^--N), hcp-Ru$_1$Co delivers Y_{NH_3} of 11.65 ± 0.46 mg h^{-1} cm^{-2} at −0.1 V and FE_{NH_3} of 100% at 0 V (Supplementary Fig. 34). These metrics position it among the most active metal-based catalysts for NO_3RR (Supplementary Table 4).

EC and NH_3 production cost analyses are explored only considering the price of renewable electricity (0.03 $\$_{USD}$ kWh^{-1}, full levelized cost of electricity for utility solar power according to the announcement by the US Department of Energy for the 2030

https://doi.org/10.1038/s41467-025-61232-z

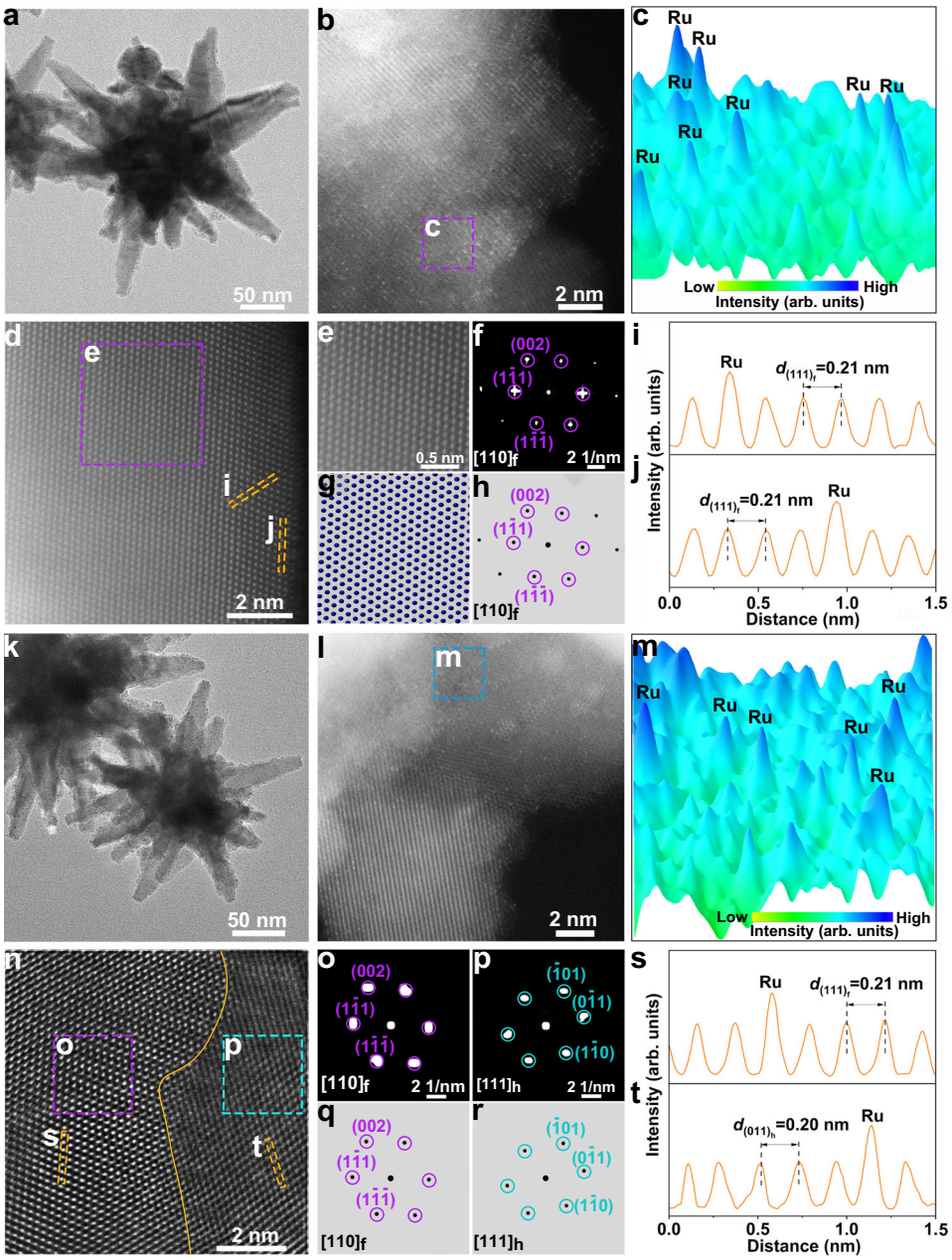

Fig. 3 | Characterization of fcc-Ru_1Co and hcp/fcc-Ru_1Co. a TEM image of fcc-Ru_1Co. **b** AC-HAADF-STEM image of fcc-Ru_1Co. **c** 3D surface plots converted from the purple square in (**b**). **d** High-resolution AC-HAADF-STEM image of fcc-Ru_1Co. **e** Enlarged HAADF-STEM image extracted from the purple square in (**d**). **f** The corresponding FFT pattern. **g** and **h** The simulated atomic model (**g**) and the electron diffraction pattern (**h**) of fcc-Co oriented along the [110] zone axis. **i** and **j** Intensity profiles from the orange rectangles in (**d**). **k** TEM image of hcp/fcc-Ru_1Co. **l** AC-HAADF-STEM image of hcp/fcc-Ru_1Co. **m** 3D surface plots extracted from the blue square in (**h**). **n** High-resolution AC-HAADF-STEM image of hcp/fcc-Ru_1Co. **o** and **p** FFT patterns extracted from the squares in (**n**). **q** and **r** The simulated electron diffraction patterns oriented along the $[110]_{fcc}$ and $[111]_{hcp}$ zone axes. **s** and **t** Intensity profiles from the rectangles in (**n**). Source data for this figure are provided as a Source Data file.

target)[23–25]. As shown in Supplementary Fig. 35 and Fig. 5d, EC and NH_3 production cost of hcp-Ru_1Co are calculated as 19.04 ± 1.10 kWh kg^{-1} and 0.57 ± 0.03 $\$_{USD}$ kg^{-1} at 0.1 V, respectively, significantly lower than those of hcp/fcc-Ru_1Co (37.0 ± 0.37 kWh kg^{-1}, 1.11 ± 0.01 $\$_{USD}$ kg^{-1}) and fcc-Ru_1Co (288.78 ± 0.50 kWh kg^{-1}, 8.66 ± 0.02 $\$_{USD}$ kg^{-1}). Notably, the EC values of hcp-Ru_1Co at all potentials are significantly lower than commercial benchmarks (1–1.5 $\$ kg^{-1}$)[26], highlighting its industrial viability. Temperature-dependent Y_{NH_3} measurements reveal the apparent activation energy (E_a) of 3.49 kJ mol^{-1} for hcp-Ru_1Co, significantly lower than that of hcp/fcc-Ru_1Co (14.22 kJ mol^{-1}) and fcc-Ru_1Co (25.55 kJ mol^{-1}), confirming the accelerated NO_3RR kinetics (Fig. 5e and Supplementary Fig. 36). In addition, hcp-Ru_1Co possesses a larger electrochemically active surface area (ECSA) compared to hcp/fcc-Ru_1Co and fcc-Ru_1Co (Supplementary Fig. 37, Table 5), consistent with the N_2 adsorption–desorption results (Supplementary Fig. 38). Y_{NH_3} values normalized to ECSA and Brunauer–Emmett–Teller (BET) surface area indicate the superior intrinsic activity of hcp-Ru_1Co (Supplementary Figs. 39 and 40). Electrochemical impedance spectroscopy (EIS) reveals reduced charge transfer impedance for hcp-Ru_1Co, attributed to its distinctive hcp structure and large ECSA (Supplementary Fig. 41).

https://doi.org/10.1038/s41467-025-61232-z

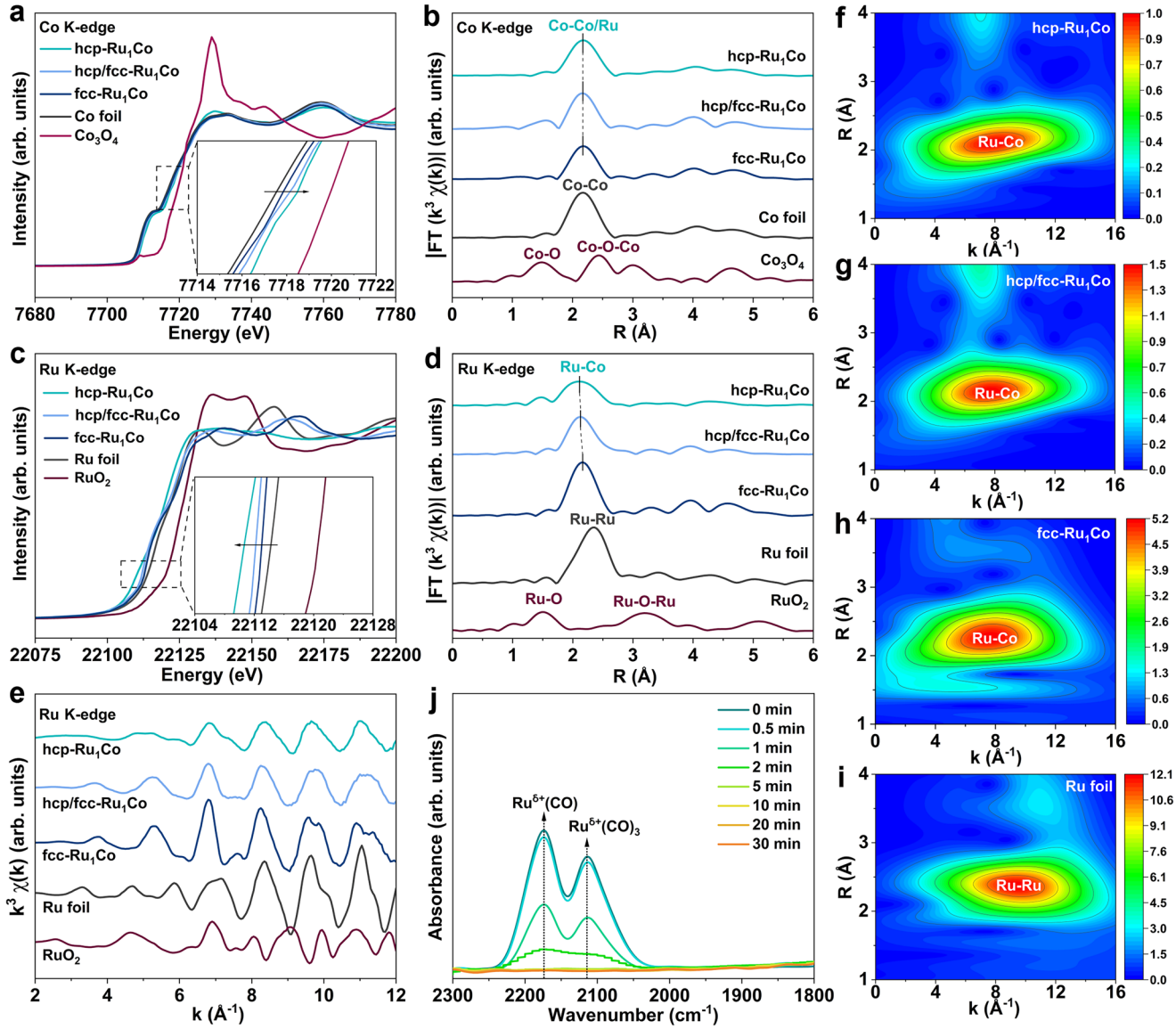

Fig. 4 | Chemical state and coordination environment. a The normalized Co K-edge XANES spectra of hcp-Ru_1Co, hcp/fcc-Ru_1Co, fcc-Ru_1Co, Co foil, and Co_3O_4. **b** The Co K-edge FT-EXAFS spectra of hcp-Ru_1Co, hcp/fcc-Ru_1Co, fcc-Ru_1Co, Co foil, and Co_3O_4. **c** The normalized Ru K-edge XANES spectra of hcp-Ru_1Co, hcp/fcc-Ru_1Co, fcc-Ru_1Co, Ru foil, and RuO_2. **d** The Ru K-edge FT-EXAFS spectra of hcp-Ru_1Co, hcp/fcc-Ru_1Co, fcc-Ru_1Co, Ru foil, and RuO_2. **e** The Ru K-edge EXAFS spectra of hcp-Ru_1Co, hcp/fcc-Ru_1Co, fcc-Ru_1Co, Ru foil, and RuO_2. **f-i** The WT-EXAFS contour plots of hcp-Ru_1Co (**f**), hcp/fcc-Ru_1Co (**g**), fcc-Ru_1Co (**h**), and Ru foil (**i**) at Ru K-edge. **j** In situ CO-DRIFTS spectra of hcp-Ru_1Co at room temperature. Source data for this figure are provided as a Source Data file.

To verify that the produced NH_3 originates from the NO_3RR process catalyzed by hcp-Ru_1Co, control experiments are carried out. Negligible NH_3 is detected in solutions of 0.5 M Na_2SO_4 and 0.1 M NaOH at 0 V or in solutions of 0.5 M Na_2SO_4 and 0.1 M NaOH with 200 ppm NO_3^--N at open circuit potential (OCP), and using pure NF substrate as the working electrode (Supplementary Fig. 42). ^{15}N isotope labeling experiments employing $^{15}NO_3^-$ as nitrogen source yield characteristic $^{15}NH_4^+$ peaks at $\delta = 6.91$ and 7.06 ppm in ^1H nuclear magnetic resonance (NMR) spectrum (Supplementary Fig. 43), confirming NH_3 generation through NO_3RR (Supplementary Fig. 44). Y_{NH_3} values obtained from ^1H NMR method match those from colorimetric analysis (Fig. 5f), validating both analytical methods.

Durability is a pivotal aspect in evaluating the performance of electrocatalysts. As depicted in Supplementary Fig. 45, negligible changes in Y_{NH_3} and FE_{NH_3} of hcp-Ru_1Co during 12 consecutive recycling tests demonstrate its robust electrochemical stability. Chronopotentiometric test under continuous electrolyte flow (2 mL min^{-1}, Supplementary Fig. 46) maintains stable Y_{NH_3} and FE_{NH_3} over 1200 h of prolonged operation (Fig. 5g). Post-stability characterizations confirm the retention of nano-urchin morphology, atomic Ru dispersion (Supplementary Fig. 47), crystal structure (Supplementary Fig. 48), and chemical states (Supplementary Fig. 49). In situ Raman spectroscopy during NO_3RR only detects the vibration mode of SO_4^{2-} (981 cm^{-1}) from electrolyte (Fig. 5h, Supplementary Fig. 50)[27]. No additional Raman peaks are observed at all applied potentials, suggesting that hcp-Ru_1Co does not transform into oxide during NO_3RR. Furthermore, hcp-Ru_1Co exhibits competitive performance across a broad range of NO_3^--N concentrations (100–500 ppm), suggesting its wide applicability (Supplementary Fig. 51). As current density increases from 50 to 500 mA cm^{-2}, Y_{NH_3} of hcp-Ru_1Co progressively rises, attaining a maximum value of 25.52 mg h^{-1} cm^{-2} at 500 mA cm^{-2} (Supplementary Fig. 52).

https://doi.org/10.1038/s41467-025-61232-z

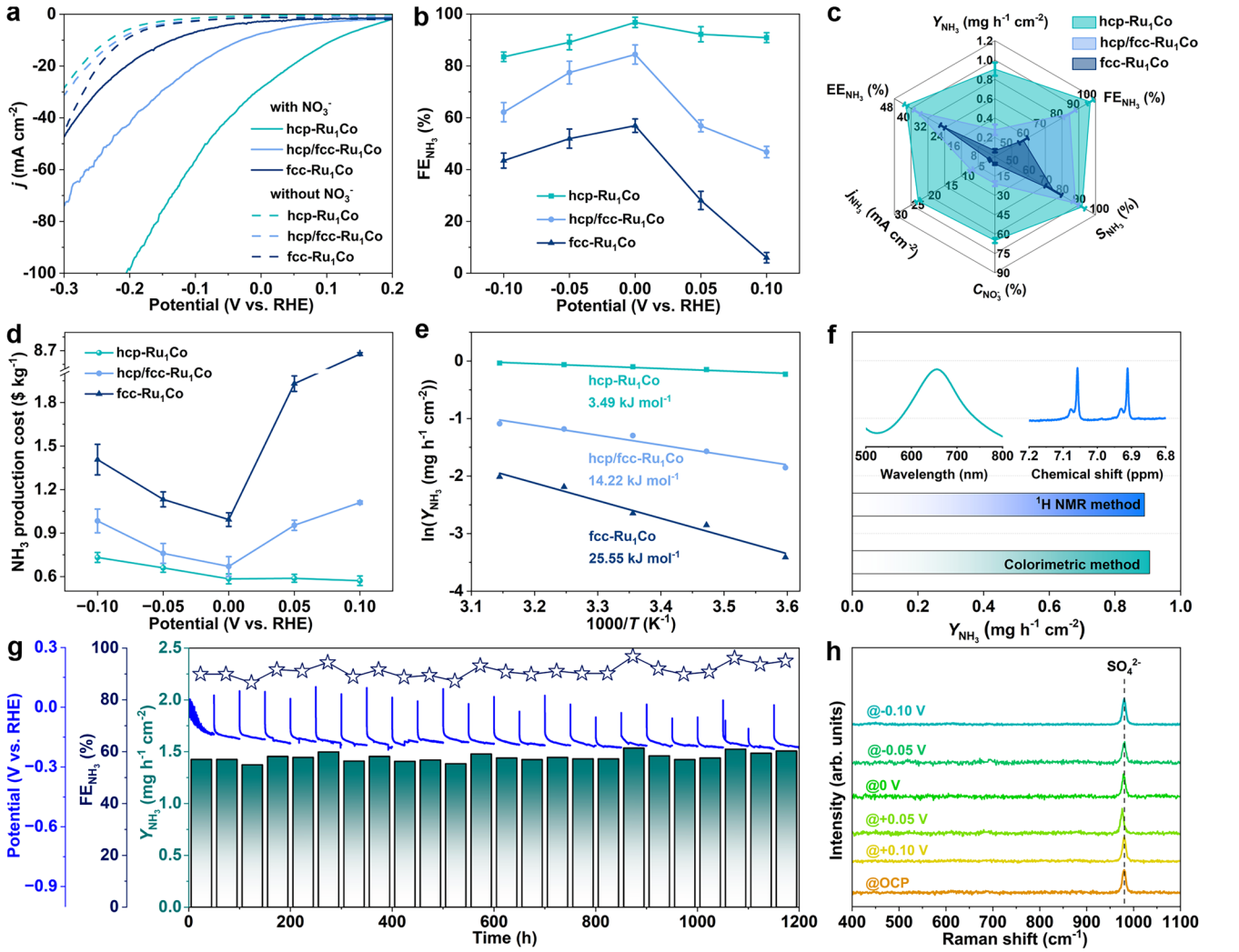

Fig. 5 | Electrocatalytic NO_3RR performance. a LSV curves of hcp-Ru_1Co, hcp/fcc-Ru_1Co, and fcc-Ru_1Co at a scan rate of 5 mV s^{-1} in an electrolyte containing 0.5 M Na_2SO_4 and 0.1 M NaOH with and without 200 ppm NO_3^--N at room temperature (25 °C). **b** FE_{NH_3} of hcp-Ru_1Co, hcp/fcc-Ru_1Co, and fcc-Ru_1Co at different potentials. **c** Comparison of Y_{NH_3}, FE_{NH_3}, $C_{NO_3^-}$, S_{NH_3}, j_{NH_3}, and EE_{NH_3} over hcp-Ru_1Co, hcp/fcc-Ru_1Co, and fcc-Ru_1Co at 0 V. **d** NH_3 production cost of hcp-Ru_1Co, hcp/fcc-Ru_1Co, and fcc-Ru_1Co at different potentials. **e** E_a of hcp-Ru_1Co, hcp/fcc-Ru_1Co, and fcc-Ru_1Co at 0 V. **f** Y_{NH_3} of hcp-Ru_1Co at 0 V obtained by colorimetric and ^{1}H NMR methods (the insets are UV–Vis absorption and ^{1}H NMR spectra of post-electrolyzed solution over hcp-Ru_1Co at 0 V). **g** Chronopotentiometry curve of hcp-Ru_1Co in an H-type continuous-flow cell at 20 mA cm^{-2} with corresponding Y_{NH_3} and FE_{NH_3}. **h** In situ Raman spectra of hcp-Ru_1Co during chronopotentiometry test at different potentials in an electrolyte containing 0.5 M Na_2SO_4 and 0.1 M NaOH with 200 ppm NO_3^--N. All potentials are referenced to the RHE scale without iR compensation. Catalyst loading amount for all NO_3RR tests is 3 mg cm^{-2}. Error bars represent the standard deviations from three independent measurements. Source data for this figure are provided as a Source Data file.

Mechanistic studies

Recent studies have highlighted the critical role of catalyst surface potential in regulating NO_3^- adsorption, where elevated surface potentials significantly enhance NO_3^- adsorption and improve NO_3RR performance[28–30]. To explore the surface potential of Ru_1Co SAAs, Kelvin probe force microscopy (KPFM) is conducted (Fig. 6a). The average surface potential of hcp-Ru_1Co achieved by contact potential difference is 155 mV, substantially exceeding that of hcp/fcc-Ru_1Co (100 mV) and fcc-Ru_1Co (44 mV) (Fig. 6b). This enhanced surface potential of hcp-Ru_1Co, attributed to its unique hcp structure, facilitates NO_3^- adsorption and thereby accelerates the reaction kinetics. To quantitatively assess NO_3^- adsorption behavior, Ru_1Co SAAs are immersed in an electrolyte containing 200 ppm NO_3^--N and agitated for 30 min, the NO_3^- adsorption capacity (q_e) is determined by measuring the concentration of NO_3^- in solution before and after agitation. As shown in Supplementary Fig. 53, hcp-Ru_1Co achieves a q_e value of 1.91 ± 0.05 μmol $mg_{cat.}^{-1}$, significantly surpassing hcp/fcc-Ru_1Co (1.20 ± 0.03 μmol $mg_{cat.}^{-1}$) and fcc-Ru_1Co (0.77 ± 0.02 μmol $mg_{cat.}^{-1}$). Furthermore, Fourier transform infrared (FT-IR) analysis of Ru_1Co SAAs with absorbed NO_3^- further confirms the enhanced NO_3^- adsorption on hcp-Ru_1Co, evidenced by intensified absorption at 1350 cm^{-1} corresponding to anti-symmetric stretching vibrations of NO_3^- (Supplementary Fig. 54)[31]. These findings collectively demonstrate that hcp-Ru_1Co possesses a stronger NO_3^- adsorption, contributing to its enhanced NO_3RR performance.

To probe into the intermediates formed during the NO_3RR process, in situ attenuated total reflection surface-enhanced infrared absorption spectroscopy (ATR-SEIRAS, Supplementary Fig. 55) and online differential electrochemical mass spectrometry (DEMS, Supplementary Fig. 56) are carried out. In situ ATR-SEIRAS spectra of hcp-Ru_1Co (Fig. 6c) display characteristic peaks at 1595, 1483, 1438, 1235, and 1168 cm^{-1}, attributed to the vibrations of *NO, $*NH_3$, $*NH_2$, $*NO_2$, and $*NH_2OH$, respectively[32,33]. The peak at 1668 cm^{-1} is assigned to the bending vibration of the adsorbed H_2O[34]. Online DEMS analysis during

https://doi.org/10.1038/s41467-025-61232-z

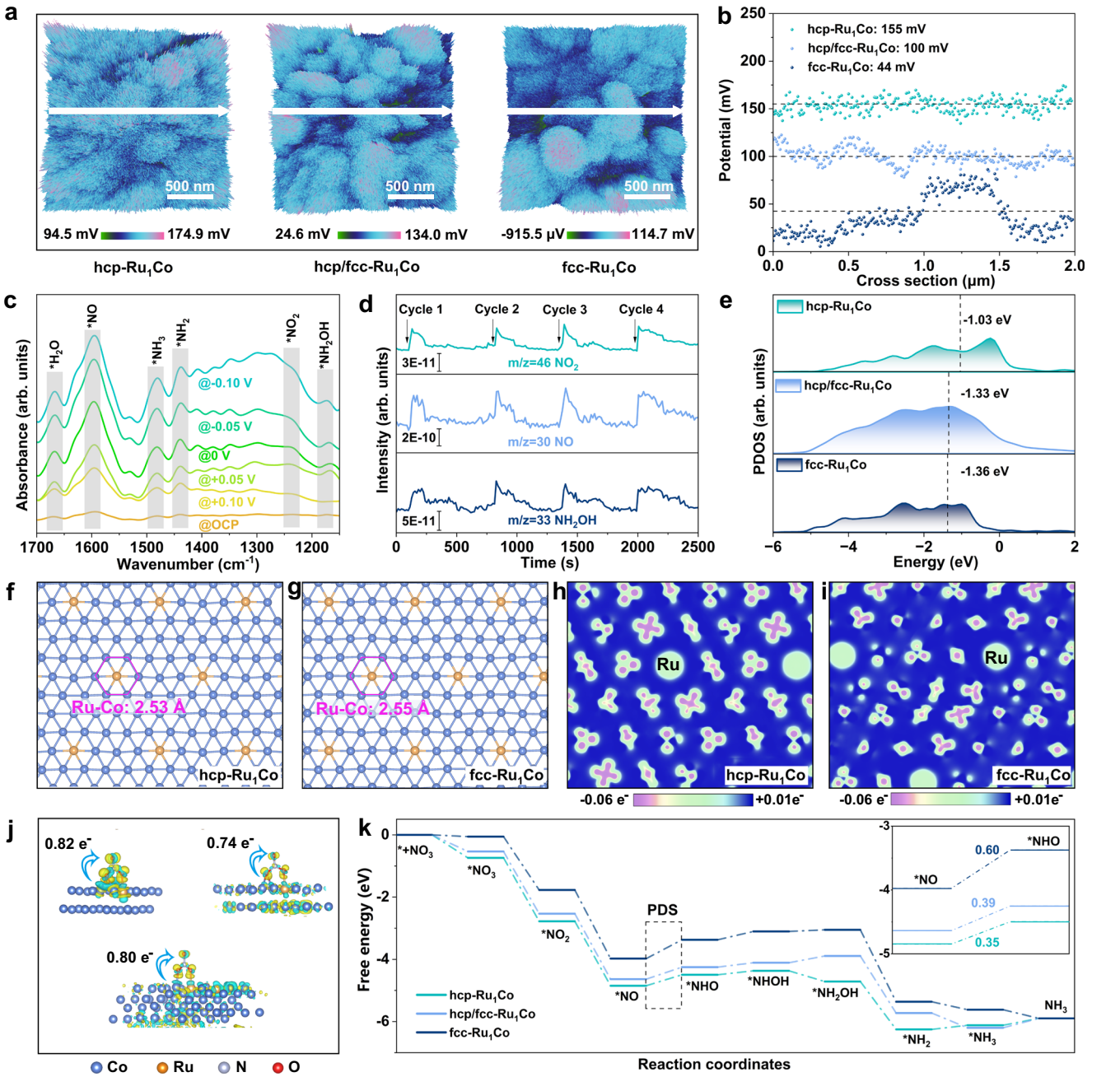

Fig. 6 | Mechanistic studies. a Surface potential distribution of hcp-Ru_1Co, hcp/fcc-Ru_1Co, and fcc-Ru_1Co. **b** The corresponding surface potentials. **c** In situ ATR-SEIRAS spectra of hcp-Ru_1Co at different potentials. **d** Online DEMS spectra of hcp-Ru_1Co during the NO_3RR process. **e** The PDOS profiles of hcp-Ru_1Co, hcp/fcc-Ru_1Co, and fcc-Ru_1Co. The vertical dashed lines indicate the position of the *d*-band center. **f** and **g** The optimized structure models of hcp-Ru_1Co (**f**) and fcc-Ru_1Co (**g**). **h** and **i** 2D deformation charge density difference maps of hcp-Ru_1Co (**h**) and fcc-Ru_1Co (**i**). **j** The charge density difference of $*NO_3$ adsorbed on hcp-Ru_1Co, hcp/fcc-Ru_1Co, and fcc-Ru_1Co (electron accumulation and depletion are indicated by yellow and cyan regions, respectively). **k** The free energy diagrams of NO_3RR over hcp-Ru_1Co, hcp/fcc-Ru_1Co, and fcc-Ru_1Co. Source data for this figure are provided as a Source Data file.

chronoamperometry test at 0 V reveals the mass signals of mass-to-charge ratios (*m/z*) of 46, 33, 32, 31, 30, and 17, attributed to $*NO_2$, $*NH_2OH$, *NHOH, *NHO, *NO, and $*NH_3$, respectively (Fig. 6d and Supplementary Fig. 57). Based on these detected intermediates, the NO_3RR pathway is deduced, involving the following key intermediates: $*NO_3 \rightarrow *NO_2 \rightarrow *NO \rightarrow *NHO \rightarrow *NHOH \rightarrow *NH_2OH \rightarrow *NH_2 \rightarrow *NH_3$.

To gain preliminary insights into the enhanced NO_3RR performance of hcp-Ru_1Co, density functional theory (DFT) calculations are performed. The optimized structure models are provided in Supplementary Fig. 58 and Supplementary Data 1. Partial density of state (PDOS) profiles reveal that hcp-Ru_1Co exhibits a *d*-band center at −1.03 eV, positioned closer to the Fermi level compared to hcp/fcc-Ru_1Co (−1.33 eV) and fcc-Ru_1Co (−1.36 eV) (Fig. 6e). The upshift of the *d*-band center for hcp-Ru_1Co could theoretically favor the adsorption of intermediates. Additionally, the effect of the crystal structure on Ru–Co interatomic interaction is explored. As shown in the structure models (Fig. 6f, g), hcp-Ru_1Co possesses a relatively shorter Ru–Co bond length (2.53 Å) than fcc-Ru_1Co (2.55 Å), consistent with XAS findings. 2D deformation charge density maps and Bader charge analysis demonstrate electrons transfer from Co to Ru (Fig. 6h, i), with

hcp-Ru_1Co showing a slightly larger charge transfer, indicating an enhanced Ru–Co interatomic interaction in hcp-Ru_1Co.

Gibbs free energy of NO_3^- adsorption $\left(\Delta G_{*NO_3}\right)$ reveals that hcp-Ru_1Co exhibits a more negative ΔG_{*NO_3} of −0.74 eV compared to hcp/fcc-Ru_1Co (−0.53 eV) and fcc-Ru_1Co (−0.05 eV) (Supplementary Fig. 59, Supplementary Data 1). This suggests a stronger NO_3^- adsorption on hcp-Ru_1Co, which aligns with the results of NO_3^- adsorption capacity and FT-IR experiments in Supplementary Figs. 53 and 54. Charge density difference maps and Bader charge analysis demonstrate that 0.82 electrons are transferred from hcp-Ru_1Co to $*NO_3$, exceeding the amount transferred on hcp/fcc-Ru_1Co (0.80 electrons) and fcc-Ru_1Co (0.74 electrons) (Fig. 6j). Free energy diagrams identify the hydrogenation of *NO (*NO → *NHO) as the potential-determining step (PDS) for Ru_1Co SAAs (Fig. 6k, Supplementary Figs. 60–62, Supplementary Data 1). Notably, hcp-Ru_1Co exhibits a lower energy barrier of PDS (0.35 eV) compared to hcp/fcc-Ru_1Co (0.39 eV) and fcc-Ru_1Co (0.60 eV). Considering that HER is a primary competitive reaction, the free energy of *H adsorption is calculated (Supplementary Figs. 63, 64, Supplementary Data 1). The free energy required to generate by-product H_2 for hcp-Ru_1Co is 0.91 eV, higher than that for hcp/fcc-Ru_1Co (0.51 eV) and fcc-Ru_1Co (0.09 eV). This suggests that hcp-Ru_1Co could potentially suppress the competing HER.

The performance of the Zn-NO_3^- battery

The Zn-NO_3^- battery offers dual functionality by generating electricity while converting NO_3^- pollutants into valuable NH_3[35]. The Zn-NO_3^- battery is constructed by anchoring hcp-Ru_1Co on NF as the cathode, paired with a zinc plate anode (Supplementary Fig. 65). The hcp-Ru_1Co assembled Zn-NO_3^- battery exhibits a stable OCP of 1.405 V vs. Zn/Zn^{2+} (Supplementary Fig. 66). Two such batteries connected in series can power a bulb of 1.5 V (Supplementary Fig. 67). Additionally, the hcp-Ru_1Co assembled Zn-NO_3^- battery delivers a high power-density of 6.55 mW cm^{-2}, surpassing most recently reported Zn-NO_3^- batteries (Supplementary Fig. 68 and Table 6). At current densities of 2, 4, and 6 mA cm^{-2}, the specific capacities of this battery are 576.81, 616.84, and 668.51 mAh g^{-1}, respectively (Supplementary Fig. 69). Consequently, the corresponding energy densities under these conditions are calculated as 470.03, 448.13, and 416.04 mWh g^{-1}. The battery demonstrates high rate-capability and stable operation at current densities ranging from 1 to 20 mA cm^{-2} (Supplementary Fig. 70). Continuous discharge–charge cycling at 2 mA cm^{-2} suggests its robust stability (Supplementary Fig. 71). Additionally, it achieves an Y_{NH_3} of 1.72 ± 0.02 mg h^{-1} cm^{-2} at 50 mA cm^{-2} and a FE_{NH_3} of $90.93 \pm 0.80\%$ at 40 mA cm^{-2} (Supplementary Fig. 72). Minimal fluctuations in both Y_{NH_3} and FE_{NH_3} during consecutive recycling test at 40 mA cm^{-2} confirm robust long-term stability (Supplementary Fig. 73).

Discussion

In summary, Ru_1Co SAAs with distinct crystal phases, i.e., hcp-Ru_1Co, hcp/fcc-Ru_1Co, and fcc-Ru_1Co, are successfully synthesized through precise control of the phase transition process and exhibit crystal phase-dependent performance in NO_3RR to NH_3. Notably, hcp-Ru_1Co demonstrates superior catalytic performance with FE_{NH_3} of $96.78 \pm 1.97\%$ at 0 V, EC of 19.04 ± 1.10 kWh kg^{-1}, NH_3 production cost of 0.57 ± 0.03 $\$_{USD}$ kg^{-1}, and stable operation exceeding 1200 h, significantly outperforming hcp/fcc-Ru_1Co and fcc-Ru_1Co. Insightful experiments and theoretical calculations reveal that hcp-Ru_1Co is featured with shorter Ru–Co interatomic distances, stronger Ru–Co interatomic interactions, and more positive surface potential, which enhance the adsorption capacity of NO_3^-, reduces the free energy barrier of PDS, and suppresses the HER. Furthermore, hcp-Ru_1Co, when integrated as the cathode electrocatalyst into Zn-NO_3^- battery, demonstrates its significant potential for application in advanced energy devices. This study not only achieves precise control over the crystal phase of SAAs but also provides comprehensive insights into the relationship between the crystal structure of SAAs and catalytic performance.

Methods

Chemicals and reagents

Cobalt chloride hexahydrate ($CoCl_2 \cdot 6H_2O$, 99.0 wt%), ruthenium(III) chloride hydrate ($RuCl_3 \cdot xH_2O$, 99.95 wt%), 1,4-butanediol (98 wt%), sodium sulfate anhydrous (Na_2SO_4, 99.0 wt%), deuterium oxide (D_2O, 99.9 at% D), sodium hypochlorite solution (NaClO, available chlorine 5.5–6.5 wt%), ammonium chloride-^{15}N ($^{15}NH_4Cl$, 98.5 wt%), sodium nitrate–^{15}N ($Na^{15}NO_3$, 98.5 wt%), maleic acid ($C_4H_4O_4$, 98.0 wt%), salicylic acid ($C_7H_6O_3$, 99.5 wt%), sodium citrate dihydrate ($C_6H_5Na_3O_7 \cdot 2H_2O$, 99.0 wt%), N-(1-naphthyl) ethylenediamine dihydrochloride ($C_{12}H_{14}N_2 \cdot 2HCl$, 98 wt%), phosphoric acid (H_3PO_4, 85 wt%), sulfanilamide ($C_6H_8N_2O_2S$, 99.5 wt%), and nitroferricyanide (III) dihydrate ($Na_2Fe(CN)_5NO \cdot 2H_2O$, 99.0 wt%) were obtained from Shanghai Macklin Biochemical Co., Ltd. Sodium hydroxide (NaOH, ≥96.0 wt%), sulfuric acid (H_2SO_4, 95.0–98.0 wt%), hydrogen chloride (HCl, 36.0–38.0 wt%), and ammonium chloride (NH_4Cl, ≥99.5 wt%) were purchased from Sinopharm Chemical Reagent Co., Ltd. Ethanol (C_2H_5OH, ≥99.7 wt%) was purchased from Tianjin Fuyu Fine Chemical Co., Ltd. Acetone (C_3H_6O, ≥99 wt%) was purchased from Yantai Far East Fine Chemical Co., Ltd. Nickel foam (NF, thickness: 2 mm) was purchased from Tianjin EVS Chemical Technology Co., Ltd. Nafion solution (D520, 5 wt%, Dupont) was purchased from Suzhou Sinero Technology Co., Ltd. Nafion 211 membrane (diameter: 3 cm, thickness: 25.4 μm) was purchased from SCI Materials Hub. All reagents were utilized without further purification. Deionized water with a resistivity of 18.2 MΩ was employed throughout all experimental procedures.

Synthesis of Ru_1Co SAAs

0.08 M $CoCl_2 \cdot 6H_2O$ and 0.15 M NaOH were dissolved in 40 mL of 1,4-butanediol to form solution A. 0.015 g $RuCl_3 \cdot xH_2O$ were dissolved in 5 mL of 1,4-butanediol to form solution B. Subsequently, solution B was gradually introduced into solution A under vigorous stirring for 30 min. The mixed solution was then heated to 230 °C for 20 min. The resulting product was washed with ethanol and acetone several times, and dried under vacuum at 60 °C for 3 h. Finally, the precursor powder was annealed at 300, 500, and 700 °C for 30 min at N_2 atmosphere with a heating rate of 5 °C min^{-1} to form hcp-Ru_1Co, hcp/fcc-Ru_1Co and fcc-Ru_1Co, respectively.

Fabrication of the working electrode

The working electrode was fabricated by immobilizing Ru_1Co SAAs onto the pretreated nickel form (NF) substrate. In detail, NF was sequentially pretreated by sonication in HCl solution (3 M), followed by thorough rinsing with ethanol and deionized water to remove surface impurities. Subsequently, the synthesized sample (hcp-Ru_1Co, hcp/fcc-Ru_1Co, and fcc-Ru_1Co; 20 mg each) was dispersed in a mixed solution consisting of 950 μL ethanol and 50 μL Nafion under sonication for 0.5 h to form a homogeneous ink. Finally, the ink (300 μL) was dropped onto the surface of the pretreated NF (1×1 cm^2), and dried in air for 30 min to form the working electrode. The mass loading of the catalyst was calculated to be 3 mg cm^{-2}.

Physicochemical characterizations

XRD patterns were acquired using a Rigaku SmartLab powder diffractometer with Cu Kα radiation ($\lambda = 1.5418$ Å). TEM images were recorded using a HITACHI H-8100 electron microscope with an operation voltage of 200 kV. AC-HAADF-STEM was conducted on ThermoFisher Scientific Themis microscope (300 kV) equipped with image and probe correctors, using a beam current of 2 pA, a convergence angle of 25 mrad, and a collection angle range of 55–220 mrad

conditions. ICP-OES was carried out on an Agilent 5110 system. XPS measurements were performed on an ESCALABMK II spectrometer equipped with Mg Kα excitation. The C1*s* peak at 284.8 eV was utilized for calibration. X-ray absorption spectroscopy (XAS) was carried out at the 1W1B beamline of the Shanghai Synchrotron Radiation Facility. In situ CO-DRIFTS experiments were performed on a Bruker Tensor II infrared spectrometer. UV–Vis absorbance spectra were collected using a SHIMADZU UV-1900 spectrophotometer. ^{1}H NMR spectra were recorded on a Bruker Avance 500 MHz spectrometer. DEMS measurements were conducted on a QAS 100 system (Linglu Instruments Co. Ltd). FT-IR spectroscopy was performed using a Perkin-Elmer spectrometer. In-situ ATR-SEIRAS spectra were collected using an INVENIO S FT-IR spectrometer equipped with a liquid nitrogen-cooled mercury cadmium telluride (MCT) detector. Raman spectra were obtained using a LabRAM HR Evolution (Horiba) with a 532 nm excitation laser. KPFM images were acquired on a BRUKER Dimension Icon with ScanAsyst system. N_2 adsorption–desorption isotherms were measured on a Quantachrome NOVA-3000 instrument.

Electrochemical measurements

Electrochemical experiments were conducted in a H-type cell with a three-electrode configuration by CHI 760E electrochemical workstation (CH Instruments Inc., China). The cathodic and anodic chambers are separated by a Nafion 211 membrane (diameter: 3 cm, thickness: 25.4 μm, DuPont). Prior to use, Nafion membrane underwent sequential pretreatment. First, the membrane was immersed in a 5% H_2O_2 solution and maintained at 80 °C for 1 h to eliminate organic contaminants. Subsequently, the membrane was repeatedly rinsed with deionized water and immersed in deionized water at 80 °C for 1 h to ensure the complete removal of any residual H_2O_2. After pretreatment, the membrane was stored in deionized water under ambient conditions.

A saturated Ag/AgCl electrode and a Pt wire served as the reference and counter electrode, while nickel foam anchored with the prepared Ru_1Co SAAs (mass loading: 3 mg cm^{-2}) was used as the working electrode. All potentials were referenced to the RHE scale without iR compensation using Eq. (1):

$$E_{RHE} = E_{Ag/AgCl} + 0.197 + 0.059 \times pH \quad (1)$$

where the pH of electrolyte was measured to be 12.98 ± 0.12 using a pH meter (Mettler Toledo).

The electrolyte containing 0.5 M Na_2SO_4, 0.1 M NaOH and 200 ppm NO_3^--N, was prepared prior to the NO_3RR tests by dissolving 71.02 g of Na_2SO_4 (0.5 mol), 4.00 g of NaOH (0.1 mol), and 1.21 g of $NaNO_3$ in 1 L of deionized water within a volumetric flask. The solution was stored at room temperature (25 °C) for subsequent use. The electrolyte volume in cathodic and anodic chamber is 12.5 mL.

LSV test was performed at a scan rate of 5 mV s^{-1} at a potential range from 0.2 to −0.3 V vs. RHE at room temperature (25 °C). Potentiostatic tests were conducted at different potentials for 1 h, with a stirring rate of 1500 r.p.m. at room temperature (25 °C). After electrolysis, the electrolyte was analyzed by UV–Vis spectrophotometry. Electrochemical double-layer capacitance (C_{dl}) was assessed using cyclic voltammetry in a non-Faradaic region (−0.45 to −0.55 V vs. Ag/AgCl) at different scan rates of 10, 20, 30, 40, 50, and 60 mV s^{-1}. Electrochemical impedance spectroscopy (EIS) tests were conducted in a frequency range of 0.01 Hz–100 kHz at open circuit potential (−0.036 V vs. RHE) in an electrolyte containing 0.5 M Na_2SO_4, 0.1 M NaOH, and 200 ppm of NO_3^--N.

Determination of NO_3^--N concentration

NO_3^--N concentration was determined using UV–Vis spectrophotometry. Initially, 100 μL of cathodic electrolyte were extracted and diluted to a total volume of 10 mL. Then, 200 μL of HCl (1 M) were incorporated to the above solution. Using UV–Vis spectrophotometry, the absorption intensities at wavelengths of 220 nm (A_{220nm}) and 275 nm (A_{275nm}) were recorded. The absorbance value (A) was determined employing the equation: $A = A_{220nm} - 2 \times A_{275nm}$. The UV–Vis absorbance spectra of standard NO_3^--N solutions with known concentrations were measured for calibration, resulting in the calibration equation: $y = 0.110x + 0.031$ with an R^2 value of 0.999.

Determination of NH_4^+-N concentration

The indophenol blue method was employed to quantify NH_4^+-N concentration. Initially, 40 μL of cathodic electrolyte were obtained and diluted to a total volume of 4 mL. Subsequently, 4 mL of chromogenic agent composed of 1.0 M NaOH, 0.36 M $C_7H_6O_3$, and 0.17 M $C_6H_5Na_3O_7{\cdot}2H_2O$, 2 mL of NaClO (0.05 M), and 0.4 mL of complexing agent (1 wt% $Na_2[Fe(NO)(CN)_5]{\cdot}2H_2O$) were sequentially introduced into the aforementioned solution. Following 1 h's incubation, UV–Vis absorbance spectra were acquired, and the absorbance at 655 nm was recorded. The UV–Vis spectra of standard NH_4^+-N solutions with known concentrations were measured for calibration, resulting in the calibration equation: $y = 0.459x + 0.032$ with an R^2 value of 0.998.

Determination of NO_2^--N concentration

Initially, 50 μL of cathodic electrolyte were extracted and diluted to a total volume of 5 mL. Subsequently, 0.1 mL of color reagent composed of 12.9 mM $C_{12}H_{14}N_2{\cdot}2HCl$, 0.38 M $C_6H_8N_2O_2S$ and 2.87 M H_3PO_4, were added to the above solution. Following 10 min's incubation, UV–Vis absorbance spectra were acquired, and the absorbance at 510 nm was recorded. The UV–Vis spectra of standard NO_2^--N solutions with known concentrations were measured for calibration, resulting in the calibration equation: $y = 0.370x + 0.001$ with an R^2 value of 0.998.

Determination of N_2H_4-N concentration

N_2H_4-N concentration was determined by the Watt and Chrisp method. Initially, a colorimetric reagent was prepared by dissolving 5.99 g $C_9H_{11}NO$ (0.01 mol) in a mixture of HCl (30 mL) and ethanol (300 mL). Subsequently, 5 mL of cathodic electrolyte were extracted and combined with 5 mL of the prepared color reagent. Following 10 min's incubation at room temperature, UV–Vis absorbance spectra were acquired, and the absorbance at 455 nm was recorded. The UV–Vis spectra of standard N_2H_4-N solutions with known concentrations were tested for calibration, resulting in the calibration equation: $y = 0.773x + 0.026$ with an R^2 value of 0.997.

Performance evaluation

To calculate NO_3^- conversion ($C_{NO_3^-}$), Eq. (2) is used as follows:

$$C_{NO_3^-} = \frac{\Delta c_{NO_3^- - N}}{C_0} \times 100\% \quad (2)$$

where c_0 represents the initial concentration of NO_3^--N in electrolyte, $\Delta c_{NO_3^- - N}$ stands for the variation in the concentration of NO_3^--N before and after electrolysis.

To calculate NH_3 selectivity (S_{NH_3}), Eq. (3) is used as follows:

$$S_{NH_3} = \frac{c_{NH_3 - N}}{\Delta c_{NO_3^- - N}} \times 100\% \quad (3)$$

where $\Delta c_{NO_3^- - N}$ is the variation in the concentration of NO_3^--N before and after electrolysis, $c_{NH_3 - N}$ stands for the concentration of $NH_3 - N$ after electrolysis.

To calculate NH_3 yield rate (Y_{NH_3}), Eq. (4) is employed as below:

$$Y_{NH_3} = \frac{c_{NH_3} \times V}{t \times S} \quad (4)$$

where c_{NH_3} stands for the concentration of NH_3 after electrolysis, V is the cathodic electrolyte volume, t represents the reduction time, S is the geometric area of the working electrode.

To calculate NH_3 Faradaic efficiency (FE_{NH_3}), Eq. (5) is used as follows:

$$FE_{NH_3} = \frac{8 \times F \times c_{NH_3} \times V}{17 \times Q} \times 100\% \quad (5)$$

where F stands for the Faradaic constant (96,485 C mol^{-1}), c_{NH_3} is the concentration of NH_3 after electrolysis, V is the cathodic electrolyte volume, and Q is the total charge that has passed through the electrode.

To calculate NO_2^- yield rate ($Y_{NO_2^-}$), Eq. (6) is employed as follows:

$$Y_{NO_2^-} = \frac{c_{NO_2^-} \times V}{t \times S} \quad (6)$$

where $c_{NO_2^-}$ stands for the concentration of NO_2^- after electrolysis, V represents the cathodic electrolyte volume, t is the reduction time in h, and S is the geometric area of the working electrode.

To calculate NO_2^- selectivity ($S_{NO_2^-}$), Eq. (7) is used as follows:

$$S_{NO_2^-} = \frac{c_{NO_2^- - N}}{\Delta c_{NO_3^- - N}} \times 100\% \quad (7)$$

where $\Delta c_{NO_3^- - N}$ is the variation in the concentration of NO_3^--N before and after electrolysis, $c_{NO_2^- - N}$ is the concentration of NO_2^--N after electrolysis.

To calculate NO_2^- Faradaic efficiency ($FE_{NO_2^-}$), Eq. (8) is used as follows:

$$FE_{NO_2^-} = \frac{2 \times F \times c_{NO_2^-} \times V}{46 \times Q} \times 100\% \quad (8)$$

where F stands for the Faradaic constant, $c_{NO_2^-}$ is the concentration of NO_2^- after electrolysis, V is the cathodic electrolyte volume, Q is the total charge that has passed through the electrode.

N_2 selectivity (S_{N_2}) is obtained by the subtraction method (Eq. 9), as only the N-containing products of NO_2^-, N_2, and NH_3 can be detected during the NO_3RR process.

$$S_{N_2} = \frac{\Delta c_{NO_3^- - N} - c_{NO_2^- - N} - c_{NH_3 - N}}{\Delta c_{NO_3^- - N}} \quad (9)$$

where $\Delta c_{NO_3^- - N}$ is the variation in the concentration of NO_3^--N before and after electrolysis, $c_{NO_2^- - N}$ is the concentration of NO_2^--N after electrolysis, $c_{NH_3 - N}$ is the concentration of $NH_3 - N$ after electrolysis.

To calculate N_2 Faradaic efficiency (FE_{N_2}), Eq. (10) is used as follows:

$$FE_{N_2} = \frac{5 \times F \times S_{N_2} \times \Delta c_{NO_3^- - N} \times V}{14 \times Q} \times 100\% \quad (10)$$

where F is the Faradaic constant (96485 C mol^{-1}), $\Delta c_{NO_3^- - N}$ is the variation in the concentration of NO_3^--N before and after electrolysis, V is the cathodic electrolyte volume, Q is the total charge that has passed through the electrode.

H_2 was detected by the gas chromatograph (GC, A91 Plus PANNA) equipped with a thermal conductivity detector (TCD). The gas effluent from the cathodic chamber was directly delivered into the gas sampling loop of GC. H_2 Faradaic efficiency (FE_{H_2}) is calculated using the following Eq. (11)[36]:

$$FE_{H_2} = \frac{2 \times F \times V_{H_2} \times G \times t \times P_0}{R \times T \times Q \times 10^6} \times 100\% \quad (11)$$

where F is the Faradaic constant (96,485 C mol^{-1}), V_{H_2} is the volume concentration of H_2 in the exhausted gas from cathodic chamber at a given sampling time (vol%), G is total gas flow rate at room temperature and ambient pressure (20 L min^{-1}), t is the electrolysis time, P_0 is the gas pressure (1.013×10^5 Pa), R is the ideal gas constant (8.314 J mol^{-1} K^{-1}), T is the temperature (298 K), and Q is the total charge that has passed through the electrode during the NO_3RR process.

To calculate NH_3 partial current density (j_{NH_3}), Eq. (12) is employed as follows:

$$j_{NH_3} = \frac{FE_{NH_3} \times Q}{t \times S} \quad (12)$$

where Q is the total charge that has passed through the electrode, t is the reduction time, and S stands for the geometric area of the working electrode.

The half-cell energy efficiency (EE_{NH_3}) determined by the ratio of fuel energy to the electrical power applied, is calculated using Eq. (13) as follows:

$$EE_{NH_3} = \frac{\left(1.23 - E^0_{NH_3}\right) \times FE_{NH_3}}{1.23 - E} \quad (13)$$

where $E^0_{NH_3}$ is the equilibrium potential of the NO_3RR process (0.69 V), E stands for the applied potential.

To calculate energy consumption (EC), Eq. 14 is employed as follows:

$$EC = \frac{(1.23 - E) \times i \times t}{m} \quad (14)$$

where E stands for the applied potential, i represents the current, t is the reduction time, m is the mass of produced NH_3 after electrolysis.

To calculate NH_3 production cost, Eq. (15) is employed as below:

$$NH_3 \text{production cost} = 0.03 \times EC \quad (15)$$

where EC stands for the energy consumption, 0.03 ($\$_{USD}$ kWh^{-1}) is the full levelized cost of electricity (LCOE) for utility solar power according to the recent announcement by the US Department of Energy (DOE) for the 2030 target[23,37]. Note that this is a simplified calculation method that solely considers the electrical price without taking into account the capital costs and Ohmic losses.

Calculation of ECSA and ECSA-normalized Y_{NH_3}

To calculate ECSA, Eq. (16) is used as follows:

$$ECSA = \frac{C_{dl}}{C_s} \quad (16)$$

where C_s refers to the specific capacitance of a flat metallic surface[38], with a value of 40 μF cm^{-2}. C_{dl} is the double-layer capacitance, which can be derived from cyclic voltammetry (CV) performed within the non-Faradaic potential range at different scan rates (10–60 mV s^{-1}). The calculation of C_{dl} is based on Eq. (17) as follows:

$$C_{dl} = \frac{\Delta i}{2 \times \upsilon} = \frac{i_a - i_c}{2 \times \upsilon} \quad (17)$$

where i_a and i_c represent the anodic and cathodic current at a certain potential, respectively, υ is the scan rate of CV.

ECSA-normalized Y_{NH_3} is calculated using Eq. (18) as follows:

$$\text{ECSA} - \text{normalized} Y_{NH_3} = \frac{c_{NH_3} \times V}{t \times \text{ECSA}} \quad (18)$$

where V stands for the cathodic electrolyte volume, t is the reduction time, c_{NH_3} is the concentration of NH_3 after electrolysis.

Calculation of BET surface area-normalized Y_{NH_3}

Y_{NH_3} is normalized to BET surface area according to the following Eq. (19):

$$\text{BET surface area} - \text{normalized} Y_{NH_3} = \frac{c_{NH_3} \times V}{t \times \text{BET surface area}} \quad (19)$$

where V stands for the cathodic electrolyte volume, t represents the reduction time, c_{NH_3} is the concentration of NH_3 after electrolysis. BET surface area is obtained by N_2 adsorption-desorption method.

In situ Raman measurement

Gamry Refence 3000 coupled with an iRaman instrument equipped with a 532 nm laser was employed for in situ Raman measurement. A self-made cell featuring a three-electrode configuration was employed. The electrolyte contained 0.5 M Na_2SO_4, 0.1 M NaOH, and 200 ppm NO_3^--N. All Raman spectra were acquired during chronoamperometric experiments.

In situ ATR-SEIRAS measurement

For in situ ATR-SEIRAS measurements, hcp-Ru_1Co was supported on an Au-coated Si crystal substrate as the working electrode, Ag/AgCl and Pt foil functioned as the reference and counter electrodes, respectively. During chronoamperometry experiments at various potentials, spectral data were collected. The electrolyte contained 0.5 M Na_2SO_4, 0.1 M NaOH, and 200 ppm NO_3^--N.

Online DEMS measurement

For online DEMS measurements, a peristaltic pump was utilized to continuously flow the electrolyte (0.5 M Na_2SO_4, 0.1 M NaOH, and 200 ppm NO_3^--N) into a custom-made electrochemical cell, in which hcp-Ru_1Co loaded on glassy carbon electrode served as the working electrode, while Pt wire and Ag/AgCl were used as the counter and the reference electrodes, respectively. Ar gas was bubbled into the electrolyte constantly before and during the DEMS measurement. The gaseous products generated from the working electrode were brought into a mass spectrometer through a hydrophobic polytetrafluoroethylene (PTFE) membrane (porosity ≥50%, pore diameter ≤20 nm). Chronoamperometry test at 0 V was carried out for 150 s. Once the test was completed and mass signals recovered to their initial levels, the subsequent cycle was initiated under identical conditions. Following four cycles, the measurement was finished.

Isotope labeling experiments

Isotopic labeling experiments utilized $Na^{15}NO_3$ (98.5 wt%) as the nitrogen source. The post-electrolysis electrolyte was extracted and adjusted to pH 4 using H_2SO_4. For ^1H NMR test, 1 mL of D_2O with 4.4 mg of $C_4H_4O_4$ was incorporated into 10 mL of the above solution. The ^1H NMR spectra of standard $^{15}NH_4^+$ solution with known concentrations were measured for calibration, resulting in the calibration equation: $y = 0.016x - 0.034$ with an R^2 value of 0.997.

NO_3^- adsorption and FT-IR experiments

To ascertain the adsorption capacities of NO_3^-, Ru_1Co SAAs (10 mg) were immersed in 10 mL of an electrolyte comprising 0.5 M Na_2SO_4, 0.1 M NaOH, and 200 ppm NO_3^--N. After stirring for 30 min, the adsorption capacity (q_e) is determined using Eq. (20) as follows:

$$q_e = \frac{\Delta c_{NO_3^- - N} \times V}{14 \times m} \quad (20)$$

where q_e stands for the adsorption capacity, $\Delta c_{NO_3^- - N}$ is the variation in the concentration of NO_3^--N before and after stirring, V is the electrolyte volume, m is the mass loading amount of Ru_1Co SAAs.

The Ru_1Co SAAs with absorbed NO_3^- underwent sequential washing with deionized water, centrifugation, and drying. Finally, they were analyzed using FT-IR spectroscopy.

Computational details

Density functional theory (DFT) calculations were carried out using the Vienna ab-initio Simulation Package software[39,40]. The generalized gradient approximation (GGA) with the Perdew–Burke–Ernzerhof (PBE) exchange-correlation function was used, and projector augmented wave (PAW) pseudo-potentials were used to model ion-electron interactions[41–43]. A plane-wave cutoff energy basis set with a cutoff energy of 450 eV was applied. To account for van der Waals forces, the DFT-D3 method was employed[44,45]. Structural relaxations utilized a Monkhoest–Pack k-point grid of 2 × 2 × 1, with convergence thresholds set to an energy tolerance of 10^{-5} eV and force below 0.05 eV Å^{-1}. A 15 Å vacuum region was introduced along the z-axis. The free energy change (ΔG) of the reaction pathway was determined using Eq. 21 as follows:

$$\Delta G = \Delta E + \Delta \text{ZPE} - T\Delta S \quad (21)$$

where ΔE, ΔZPE, and ΔS are the variations in the reaction energy, zero-point energy change, and entropy change, respectively, T stands for the temperature.

Rechargeable Zn-NO_3^- battery measurements

For the rechargeable Zn-NO_3^- battery tests, an H-cell setup with a Nafion 211 membrane as the separator was used. The anode compartment contained 2 M KOH as the electrolyte, while the cathode compartment utilized a solution of 0.5 M Na_2SO_4, 0.1 M NaOH, and 200 ppm NO_3^--N. A polished Zn plate with a geometric area of 0.5 cm^2 served as the anode, and the cathode employed NF anchored with hcp-Ru_1Co.

Reporting summary

Further information on research design is available in the Nature Portfolio Reporting Summary linked to this article.

Data availability

The data supporting the findings of this study are available within the article and its Supplementary Information files. Source data are provided with this paper.

References

1. Lin, L. et al. Low-temperature hydrogen production from water and methanol using Pt/α-MoC catalysts. *Nature* **544**, 80–83 (2017).
2. He, T. et al. Mastering the surface strain of platinum catalysts for efficient electrocatalysis. *Nature* **598**, 76–81 (2021).
3. Ge, J. et al. Ultrathin amorphous/crystalline heterophase Rh and Rh alloy nanosheets as tandem catalysts for direct indole synthesis. *Adv. Mater.* **33**, 2006711 (2021).
4. Ma, X. et al. Heterophase intermetallic compounds for electrocatalytic hydrogen production at industrial-scale current densities. *J. Am. Chem. Soc.* **146**, 20594–20603 (2024).
5. Nguyen, Q. N. et al. Elucidating the role of reduction kinetics in the phase-controlled growth on preformed nanocrystal seeds: a case study of Ru. *J. Am. Chem. Soc.* **146**, 12040–12052 (2024).

6. Wang, L. et al. New twinning route in face-centered cubic nanocrystalline metals. *Nat. Commun.* **8**, 2142 (2017).
7. Han, Z.-K. et al. Single-atom alloy catalysts designed by first-principles calculations and artificial intelligence. *Nat. Commun.* **12**, 1833 (2021).
8. Zhang, T., Walsh, A. G., Yu, J. & Zhang, P. Single-atom alloy catalysts: structural analysis, electronic properties and catalytic activities. *Chem. Soc. Rev.* **50**, 569–588 (2021).
9. Bunting, R. J., Wodaczek, F., Torabi, T. & Cheng, B. Reactivity of single-atom alloy nanoparticles: modeling the dehydrogenation of propane. *J. Am. Chem. Soc.* **145**, 14894–14902 (2023).
10. Liu, W. et al. Highly-efficient RuNi single-atom alloy catalysts toward chemoselective hydrogenation of nitroarenes. *Nat. Commun.* **13**, 3188 (2022).
11. Kaiser, S. K. et al. Single-atom catalysts across the periodic table. *Chem. Rev.* **120**, 11703–11809 (2020).
12. He, C. et al. Single-atom alloys materials for CO_2 and CH_4 catalytic conversion. *Adv. Mater.* **36**, 2311628 (2024).
13. Wu, Z. et al. Co-catalytic metal-support interactions design on single-atom alloy for boosted electro-reduction of nitrate to nitrogen. *Adv. Funct. Mater.* **34**, 2406917 (2024).
14. Yue, J., Li, Y., Yang, C. & Luo, W. Hydroxyl-binding induced hydrogen bond network connectivity on Ru-based catalysts for efficient alkaline hydrogen oxidation electrocatalysis. *Angew. Chem. Int. Ed.* **64**, e202415447 (2025).
15. Fan, L. et al. High entropy alloy electrocatalytic electrode toward alkaline glycerol valorization coupling with acidic hydrogen production. *J. Am. Chem. Soc.* **144**, 7224–7235 (2022).
16. Kim, C. et al. Atomic-scale homogeneous Ru–Cu alloy nanoparticles for highly efficient electrocatalytic nitrogen reduction. *Adv. Mater.* **34**, 2205270 (2022).
17. Hao, J. et al. Unraveling the electronegativity-dominated intermediate adsorption on high-entropy alloy electrocatalysts. *Nat. Commun.* **13**, 2662 (2022).
18. Qiu, J.-Z. et al. Pure siliceous zeolite-supported Ru single-atom active sites for ammonia synthesis. *Chem. Mater.* **31**, 9413–9421 (2019).
19. Wang, X. et al. Atomically dispersed Ru catalyst for low-temperature nitrogen activation to ammonia via an associative mechanism. *ACS Catal.* **10**, 9504–9514 (2020).
20. Sarma, B. B. et al. Tracking and understanding dynamics of atoms and clusters of late transition metals with in-situ DRIFT and XAS spectroscopy assisted by DFT. *J. Phys. Chem. C* **127**, 3032–3046 (2023).
21. Ji, K. et al. Electrocatalytic hydrogenation of 5-hydroxymethylfurfural promoted by a Ru_1Cu single-atom alloy catalyst. *Angew. Chem. Int. Ed.* **61**, e202209849 (2022).
22. Li, Y. et al. A single site ruthenium catalyst for robust soot oxidation without platinum or palladium. *Nat. Commun.* **14**, 7149 (2023).
23. Chu, S., Cui, Y. & Liu, N. The path towards sustainable energy. *Nat. Mater.* **16**, 16–22 (2017).
24. Miller, D. M. et al. Engineering a molecular electrocatalytic system for energy-efficient ammonia production from wastewater nitrate. *Energy Environ. Sci.* **17**, 5691–5705 (2024).
25. Han, S. et al. Ultralow overpotential nitrate reduction to ammonia via a three-step relay mechanism. *Nat. Catal.* **6**, 402–414 (2023).
26. MacFarlane, D. R. et al. A roadmap to the ammonia economy. *Joule* **4**, 1186–1205 (2020).
27. Gu, Z. et al. Coordination desymmetrization of copper single-atom catalyst for efficient nitrate reduction. *Angew. Chem. Int. Ed.* **63**, e202409125 (2024).
28. Zhou, J. et al. Constructing molecule-metal relay catalysis over heterophase metallene for high-performance rechargeable zinc-nitrate/ethanol batteries. *Proc. Natl Acad. Sci. USA* **120**, e2311149120 (2023).
29. Chu, K. et al. Cation substitution strategy for developing perovskite oxide with rich oxygen vacancy-mediated charge redistribution enables highly efficient nitrate electroreduction to ammonia. *J. Am. Chem. Soc.* **145**, 21387–21396 (2023).
30. Liu, Y., Ma, J., Huang, S., Niu, S. & Gao, S. Highly dispersed copper-iron nanoalloy enhanced electrocatalytic reduction coupled with plasma oxidation for ammonia synthesis from ubiquitous air and water. *Nano Energy* **117**, 108840 (2023).
31. Zhang, R. et al. Phase engineering of high-entropy alloy for enhanced electrocatalytic nitrate reduction to ammonia. *Angew. Chem. Int. Ed.* **63**, e202407589 (2024).
32. Zhang, H. et al. Transition metal gallium intermetallic compounds with tailored active site configurations for electrochemical ammonia synthesis. *Angew. Chem. Int. Ed.* **63**, e202409515 (2024).
33. Hu, Q. et al. Ammonia electrosynthesis from nitrate using a ruthenium–copper cocatalyst system: A full concentration range study. *J. Am. Chem. Soc.* **146**, 668–676 (2024).
34. Wang, H., Dekel, D. R. & Abruña, H. D. Unraveling the mechanism of ammonia electrooxidation by coupled differential electrochemical mass spectrometry and surface-enhanced infrared absorption spectroscopic studies. *J. Am. Chem. Soc.* **146**, 15926–15940 (2024).
35. Ma, C. et al. Screening of intermetallic compounds based on intermediate adsorption equilibrium for electrocatalytic nitrate reduction to ammonia. *J. Am. Chem. Soc.* **146**, 20069–20079 (2024).
36. An, B. et al. Liquid nitrogen sources assisting gram-scale production of single-atom catalysts for electrochemical carbon dioxide reduction. *Adv. Sci.* **10**, 2205639 (2023).
37. Xia, C. et al. Confined local oxygen gas promotes electrochemical water oxidation to hydrogen peroxide. *Nat. Catal.* **3**, 125–134 (2020).
38. Nairan, A., Feng, Z., Zheng, R., Khan, U. & Gao, J. Engineering metallic alloy electrode for robust and active water electrocatalysis with large current density exceeding 2000 mA cm^{-2}. *Adv. Mater.* **36**, 2401448 (2024).
39. Kresse, G. & Furthmüller, J. Efficient iterative schemes for ab initio total-energy calculations using a plane-wave basis set. *Phys. Rev. B* **54**, 11169–11186 (1996).
40. Kresse, G. & Hafner, J. Ab initio molecular dynamics for liquid metals. *Phys. Rev. B* **47**, 558–561 (1993).
41. Hammer, B., Hansen, L. B. & Nørskov, J. K. Improved adsorption energetics within density-functional theory using revised Perdew–Burke–Ernzerhof functionals. *Phys. Rev. B* **59**, 7413–7421 (1999).
42. Perdew, J. P., Burke, K. & Ernzerhof, M. Generalized gradient approximation made simple. *Phys. Rev. Lett.* **77**, 3865–3868 (1996).
43. Blöchl, P. E. Projector augmented-wave method. *Phys. Rev. B* **50**, 17953–17979 (1994).
44. Klimeš, J., Bowler, D. R. & Michaelides, A. Van Der Waals density functionals applied to solids. *Phys. Rev. B* **83**, 195131 (2011).
45. Grimme, S., Antony, J., Ehrlich, S. & Krieg, H. A. A consistent and accurate ab initio parametrization of density functional dispersion correction (DFT-D) for the 94 elements H-Pu. *J. Chem. Phys.* **132**, 154104 (2010).

Acknowledgements

This work is supported by the Qilu Young Scholarship Funding of Shandong University. This work is also supported by the National Natural Science Foundation of China (Nos. 22005176 to A.-L.W., 92061119 to Q.L., 22305138 to Y.-C.W., 22302037 to C.-F.L.), the Natural Science Foundation of Shandong Province (ZR2020QE014 to A.L.W.), the Natural Science Foundation of Jiangsu Province (BK20200228 to A.L.W.), Innovative Team Project of Jinan (202228063 to A.-L.W.), Carbon Neutrality Research Institute Fund (CNIF20230203 to A.-L.W., CNIF20220206 to

S.Y.), the Beijing NOVA program (Z201100006820066 to Q.L., 20220484172 to Q.L.), the Fundamental Research Funds for the Central Universities (GJRC003 to Q.L.), the Guangdong Basic and Applied Basic Research Foundation (Nos. 2022A1515140051 Q.L., 2023A1515140158 to C.-F.L.), the Postdoctoral Fellowship Program of CPSF (GZC20231203 to Y.-C.W.), and the Shuimu Scholar from Tsinghua University.

Author contributions

A.-L.W. and Q.L. proposed the overall research direction and guided the project. A.-L.W., Q.L., and X.Z. conceived and designed the experiments, synthesized the materials, performed the electrochemical measurements, and drafted the manuscript. Y.-C.W. conducted the aberration-corrected HAADF-STEM characterizations. K.Q. and S.Y. carried out the theoretical calculations. L.S., J.W., Y.G., X.L., and C.-F.L. provided valuable discussions and suggestions. All authors discussed and commented on the manuscript.

Competing interests

The authors declare no competing interests.

Additional information

Supplementary information The online version contains supplementary material available at https://doi.org/10.1038/s41467-025-61232-z.

Correspondence and requests for materials should be addressed to Qipeng Lu or An-Liang Wang.

Peer review information *Nature Communications* thanks Emma Lovell, Jianping Yang, and the other, anonymous, reviewer(s) for their contribution to the peer review of this work. A peer review file is available.